PAPER

Check for updates

Preparing bulk ultrafine-microstructure high-entropy alloys *via* direct solidification

Yiping Lu, [iD]†[a] Xiaoxia Gao,†[a] Yong Dong,†[a] Tongmin Wang, [iD]*[a] Hai-Lin Chen, [iD][b] Huahai Mao[b], [iD][c] Yonghao Zhao,*[d] Hui Jiang,[a] Zhiqiang Cao,[a] Tingju Li[a] and Sheng Guo*[e]

In the past three decades, nanostructured (NS) and ultrafine-microstructure (UFM) materials have received extensive attention due to their excellent mechanical properties such as high strength. However, preparing low-cost and bulk NS and UFM materials remains to be a challenge, which limits their industrial applications. Here, we report a new strategy to prepare bulk UFM alloys *via* the direct solidification of high-entropy alloys (HEAs). As a proof of concept, we designed $AlCoCr_xFeNi$ ($1.8 \leq x \leq 2.0$) HEAs and achieved a complete UFM in bulk materials. The compositional requirements for obtaining the formation of the UFM are highly demanding, necessitating the coupling of near eutectic alloy composition and the high temperature decomposition of supersaturated primary and secondary phases. Our strategy provides a low-cost and highly efficient method to prepare bulk UFM alloys, with great potential to accelerate the engineering application of these materials.

Introduction

Bulk nanostructured (NS) and ultrafine-microstructure (UFM) materials exhibit great potential for industrial applications because of their novel properties. In comparison with coarse-grained (CG) materials, NS and UFM materials show some unique physical, chemical and mechanical properties, such as high strength and hardness, excellent friction and wear performance, enhanced diffusivity, as well as superior soft and hard magnetic properties.[1–5] In addition, numerous catalytic materials are also based on ultrafine microstructures. Literature survey indicates that the preparation methods of bulk NS and UFM metals and alloys mainly include:[1,2,6–9] (1) inert gas condensation in addition to the subsequent consolidation method, *i.e.*, firstly, condensation from the metallic vapor to form nano-particles and then consolidation of the

nano-particles using an *in situ* high pressure vacuum sintering method; (2) a mechanical milling technique, *i.e.*, preparing micro-powders with nano-grains by attrition and then consolidating by sintering methods; (3) electro-deposition methods; (4) crystallization of amorphous materials; and (5) a severe plastic deformation (SPD) method. However, due to the complexity of the above-mentioned methods, the preparation cost of NS and UFM materials is high. Moreover, the dimensions of NS and UFM specimens prepared by these methods are limited in the millimeter or centimeter range, which are much smaller than the size required for industrial applications. Finally, NS and UFM materials prepared by sintering methods generally have processing defects such as porosity and impurity, which damage their already limited plasticity. Therefore, developing new advanced preparation techniques to synthesize bulk NS and UFM materials with low-cost, in large-scale, and free of processing defects is the key for their industrial applications. The direct solidification process can satisfy these requirements, and therefore has potential for solving the problems limiting the industrial applications of NS and UFM materials.[10]

Recently, Cantor and Yeh *et al.* proposed a new alloy design concept which makes a paradigm-shift from the traditional alloy design.[11,12] These new kinds of alloys were named as high-entropy alloys (HEAs) or multi-principal-element alloys. HEAs are different from conventional alloys because they have at least four principal elements, instead of one or two principal elements as in conventional alloys. This is a breakthrough in the alloy design in the traditional physical metallurgy field,

[a]*Key Laboratory of Solidification Control and Digital Preparation Technology (Liaoning Province), School of Materials Science and Engineering, Dalian University of Technology, Dalian 116024, P.R. China. E-mail: tmwang@dlut.edu.cn; Fax: +86 411 84708940; Tel: +86 411 84709400*
[b]*Thermo-Calc Software AB, Råsundavägen 18, SE-169 67 Solna, Sweden*
[c]*Materials Science and Engineering, KTH Royal Institute of Technology, Brinellvägen 23, SE-100 44 Stockholm, Sweden*
[d]*Nano Structural Materials Center, School of Materials Science and Engineering, Nanjing University of Science and Technology, Nanjing 210094, China. E-mail: yhzhao@mail.njust.edu.cn*
[e]*Department of Industrial and Materials Science, Chalmers University of Technology, SE-41296 Gothenburg, Sweden. E-mail: sheng.guo@chalmers.se*
†These authors contributed equally to this work.

and opens up a new area for the exploration of new materials and new properties.[13–27] Previous studies have indicated that some HEAs, depending on compositions, can exhibit sluggish diffusion kinetics,[13,20–22] which results in the difficulties of precipitation and the grain growth of other phases such as intermetallic compounds from the high-entropy solid solution phase. Therefore, direct solidification might formulate NSs and UFMs in HEAs,[13,21,22,26] and provide a convenient way to prepare bulk NS and UFM alloys.

As a proof of concept, in this work, we designed $AlCoCr_xFeNi$ ($1.8 \leq x \leq 2.0$) HEAs and achieved a complete UFM in bulk materials, using the direct solidification method.

Results and discussion

XRD and SEM

Fig. 1 shows the XRD patterns of the as-cast Cr1.8 and Cr2.0 alloys. Both Cr1.8 and Cr2.0 alloys comprise a mixture of B2 and BCC (A2) solid solution phases. The SEM morphologies of the as-cast Cr1.8 and Cr2.0 alloys are presented in Fig. 2 and 3. Both Cr1.8 and Cr2.0 alloys show a typical dendritic morphology: the dendritic phase (marked as A) and the inter-den-
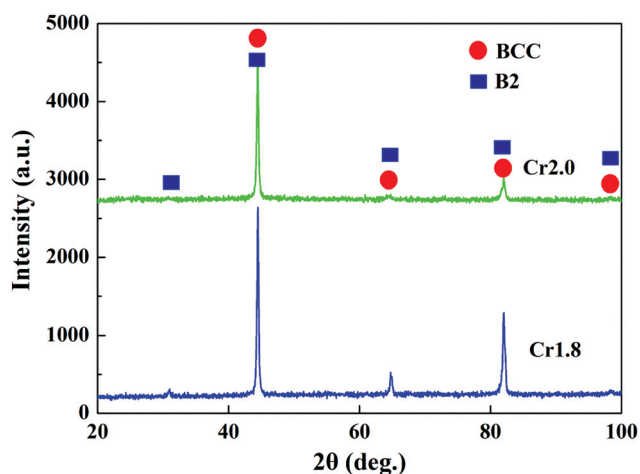
dritic region (marked as B) at low magnification are as shown in Fig. 2(a) and 3(a). The dendritic morphology is the dominant structure, with a small amount of the inter-dendritic region. Furthermore, it can be found that all of the dendritic and inter-dendritic regions have further decomposed and formed uniform UFM alloys, as revealed by the high magnification SEM micrographs in Fig. 2(b) and 3(b). Even though previous experimental studies have shown that ultrafine-grained precipitates have been often observed in the microstructure of HEAs,[13,21,22] it is believed that this is the first time the formation of a complete UFM in both dendritic and inter-dendritic regions of HEAs *via* direct solidification is reported (at present, although some nanocrystalline high-entropy alloys have been successfully prepared, they still use traditional preparation methods[28,29]). The homogeneous UFM alloys with a particle size of about 100–300 nm were observed clearly in SEM and TEM studies, as shown in Fig. 2–4. The macroscopic SEM-EDS results given in Table 1 show that the contents of elements Cr and Fe in the dendritic region are higher than those in the inter-dendritic region, while those of Al and Ni show the opposite trend. The distribution of element Co is rather uniform in both the dendritic and inter-dendritic regions. The volume fractions of the dendritic and inter-dendritic regions are ~59% and 41%, and 70% and 30% in the Cr1.8 and Cr2.0 alloys, respectively, measured by image analysis from the low magnification SEM images.

HAADF-STEM-EDS and HRTEM

In order to investigate the elemental distributions in the bulk UFM HEAs, the Cr1.8 alloy was studied using STEM-EDS mapping. Fig. 5 shows the Al, Ni, Fe, Cr and Co elemental mapping results in the dendritic region. It can be seen that the dendritic region is composed of two phases with different compositions: one is a network-like phase enriched with Ni and Al, and the other is a cylinder-shaped phase enriched with Fe and Cr. Based on the XRD results and previous results in similar alloy systems from the literature, the NiAl-rich phase has the B2 structure, while the FeCr-rich phase has the BCC structure.[30–35] This conclusion will be further supported by the following TEM results. The distribution of the element Co is quite homogeneous in these two phases.
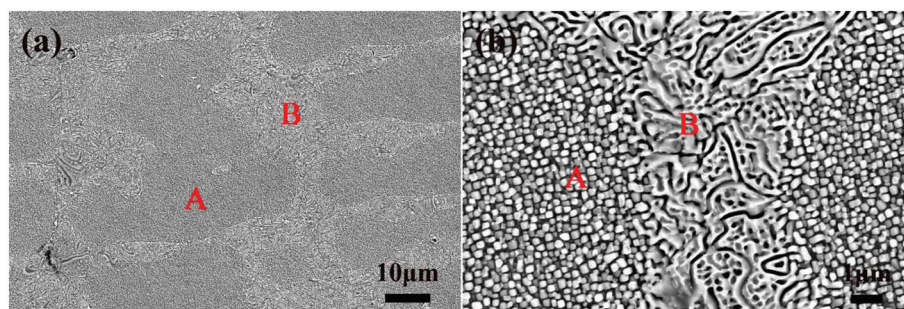

Fig. 1 X-ray diffraction patterns of the as-cast Cr1.8 and Cr2.0 HEAs.

Fig. 2 SEM images of the as-cast Cr1.8 HEA, showing a complete UFM in dendritic (A) and inter-dendritic regions (B), (a) low-magnification SEM image; (b) high-magnification SEM image.
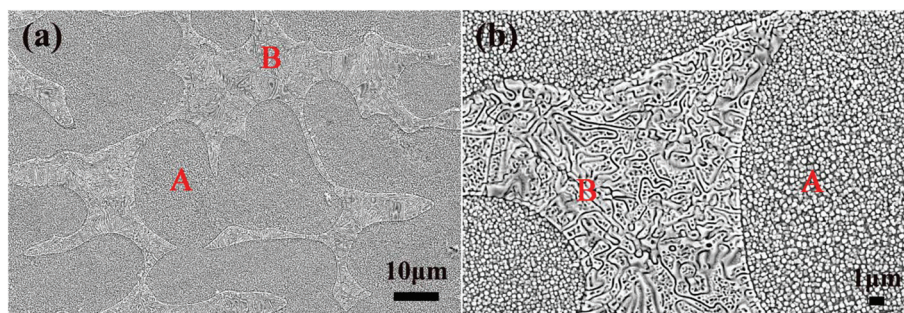
Fig. 3 SEM images of the as-cast Cr2.0 HEA, showing a complete UFM in dendritic (A) and inter-dendritic regions (B), (a) low-magnification SEM image; (b) high-magnification SEM image.
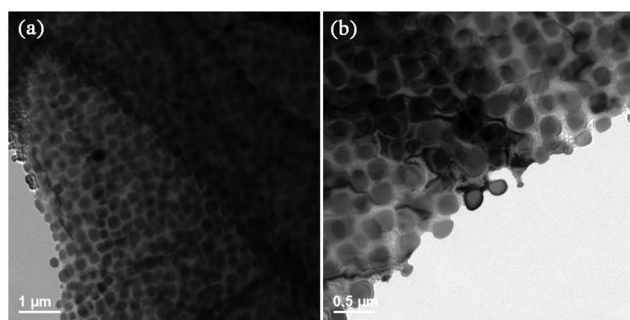
Fig. 4 TEM images of the dendritic region of the (a) Cr1.8 and (b) Cr2.0 HEAs.

Table 1 Chemical compositions of the dendritic and inter-dendritic regions of the Cr1.8 and Cr2.0 alloys, in atomic percentage

Alloys	Regions	Al	Co	Cr	Fe	Ni
Cr1.8	Dendritic	22.4	16.6	25.2	15.4	20.4
	Inter-dendritic	25.5	17.0	21.2	13.7	22.6
Cr2.0	Dendritic	18.9	16.5	31.9	15.9	16.9
	Inter-dendritic	24.0	16.1	24.9	13.6	21.8

For the Cr1.8 alloy, the inter-dendritic region is also composed of two different phases, as shown in Fig. 6, for the STEM-EDS mapping of Al, Ni, Fe, Cr and Co elements. One can see that all elements in the inter-dendritic region show distributions similar to those in the dendritic region, *i.e.*, the two phases are the NiAl-rich B2 phase and the FeCr-rich BCC phase, respectively. The micro-area chemical compositions of FeCr-rich and NiAl-rich phases in the dendritic and inter-dendritic regions of the Cr1.8 HEA were obtained by the HAADF-STEM-EDX method, as listed in Table 2. It can be seen that the FeCr-rich phase contains more Cr and Fe elements than the NiAl-rich phase. Since the Cr2.0 alloy shows a similar microstructure as that of Cr1.8, in the present paper only the Cr1.8 alloy is chosen for analysis. For the same reason, only the results from the Cr1.8 alloy are given in the following discussions to represent $AlCoCr_xFeNi$ ($1.8 \leq x \leq 2.0$) HEAs unless otherwise stated.

The structures of the B2 and BCC phases were further identified by HRTEM analyses (for the Cr1.8 alloy). Fig. 7 shows a HRTEM image of an area containing the two phases of B2 and BCC in the dendritic regions, with the electron beam parallel to ⟨001⟩ of the B2 and BCC phases. According to the corresponding fast Fourier transformation (FFT) images in Fig. 7, both B2 and BCC structures were verified.

Beyond $AlCoCr_xFeNi$ ($1.8 \leq x \leq 2.0$) HEAs

Although nanoscale phase separation in HEAs has been reported in the literature,[13,21,22,26,36,37] we, for the first time, succeeded in preparing the complete UFM bulk HEA alloys during the direct solidification process. Our large number of experiments indicated that the microstructures of $AlCoCr_xFeNi$ HEAs strongly depend on the concentration of the element Cr (the x value). At x = 1.8–2.0, complete UFM HEAs were successfully achieved, while at $x < 1.8$ or >2, such a complete UFM was not seen (Fig. 8). Obviously, too low or too high Cr contents cannot render the $AlCoCr_xFeNi$ HEAs to obtain the complete UFM.

Actually, a systematic experimental investigation was performed in this work on the variation of the content of each of the five elements (while keeping the other four elements equimolar). It was found that no complete UFM was formed in the Al-Co-Cr-Fe-Ni alloys by varying the contents of Al, Co or Ni, respectively. Alloys with optimal Fe contents, however, could also form the complete UFM. The results are similar to those with the variation of the Cr content, which are reported in the present work, and will not be discussed with more details here.

CALPHAD calculations

We turn to Calphad calculations to interpret phase stability and microstructure formation in $AlCoCr_xFeNi$ HEAs. The calculations were made using Thermo-Calc software[38] and the thermodynamic database TCHEA1.[39,40] TCHEA1 was developed especially for the material design of HEAs and multi-principal-element alloys. Applying the Calphad approach which couples the phase diagram information with thermodynamic properties, all HEAs consisting of binary and many ternary systems were critically assessed.
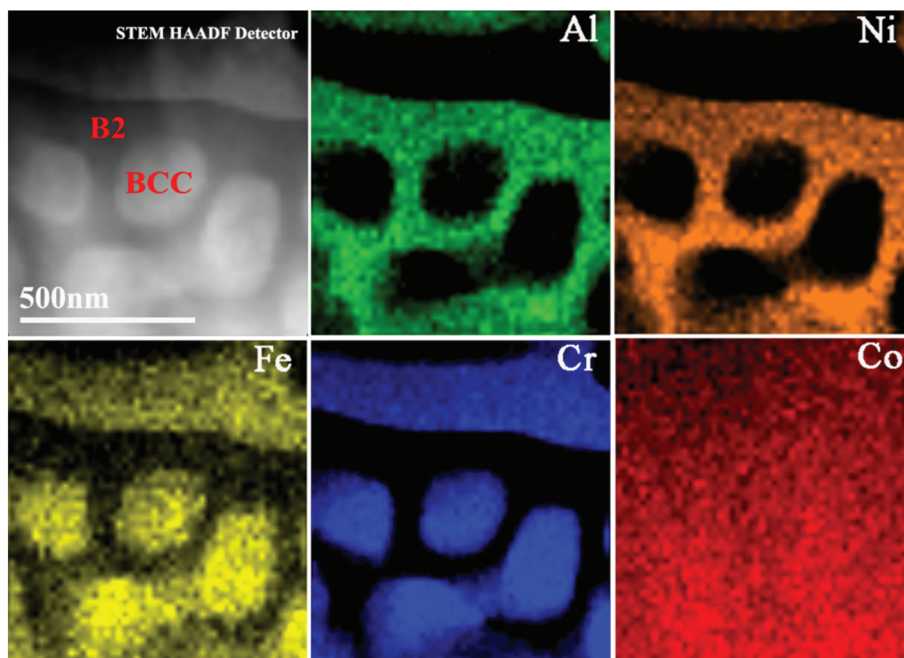
Fig. 5 HAADF-STEM-EDS elemental mappings of Al, Ni, Fe, Cr and Co in the dendritic region of the Cr1.8 alloy. The network-like B2 phase is enriched with Ni and Al, while the other cylinder-shaped BCC phase is enriched with Cr and Fe. The element Co is uniform in the whole region. The electron beam direction is close to ⟨001⟩.
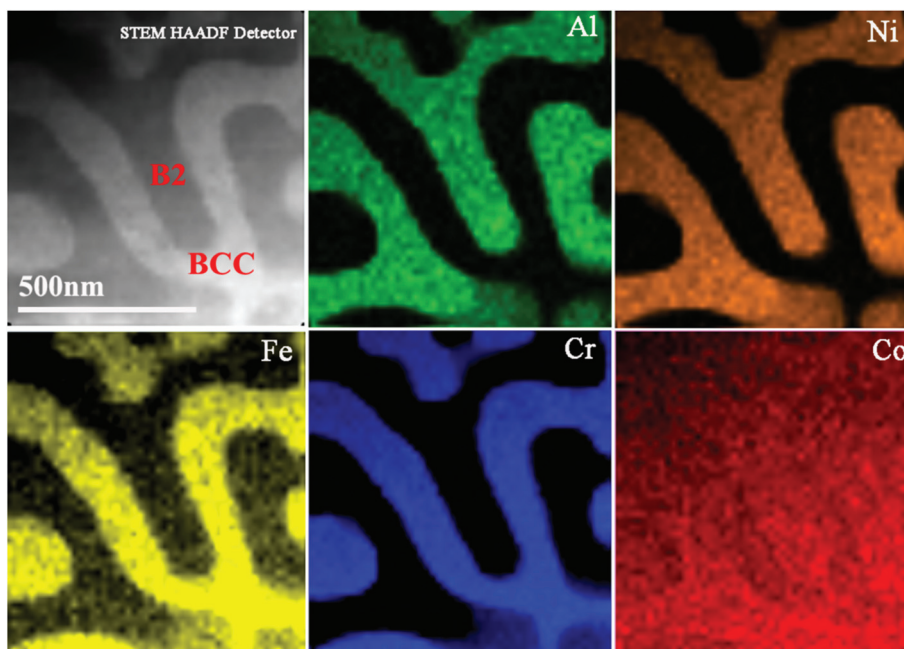
Fig. 6 HAADF-STEM-EDS elemental mappings of Al, Ni, Fe, Cr, and Co in the inter-dendritic region of the Cr1.8 alloy. The B2 phase is enriched with Ni and Al, and the BCC phase is enriched with Fe and Cr. The distribution of the Co element is uniform in the whole region. The electron beam direction is close to ⟨001⟩.

Fig. 9 presents the calculated isopleth for the alloy compositions $AlCoCr_xFeNi$ (x = 0.4–2.4). A eutectic of BCC_A2 + BCC_B2 is predicted to occur around x = 1.6, which perfectly agrees with the SEM image (Fig. 8) of the as-cast alloy Cr1.6.

Cr1.6 is fully composed of fine eutectic microstructures and is thus believed to be right at the eutectic composition.
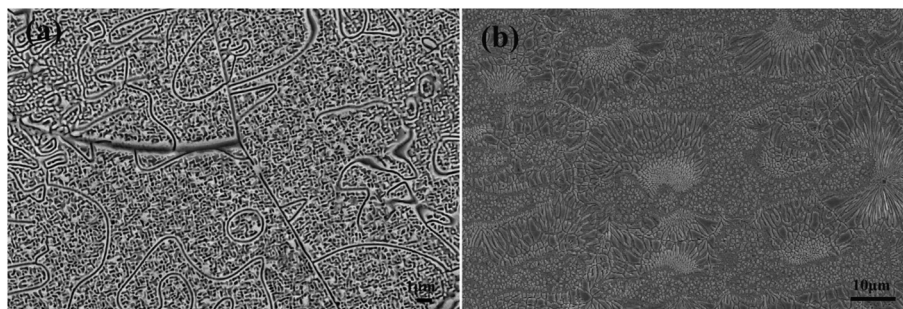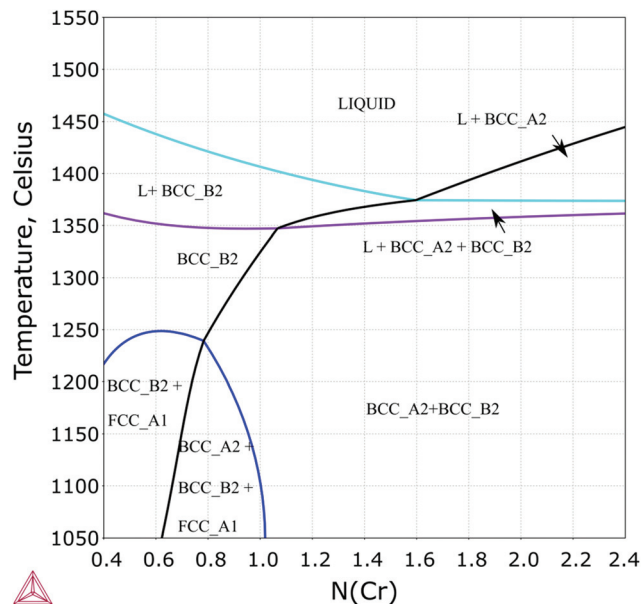
According to Fig. 9, the primary solidification phase is B2 in alloys with a lower Cr content (x < 1.6), and A2 in those with

Table 2 Micro-area chemical compositions of the FeCr-rich and NiAl-rich phases of the Cr1.8 alloy, in atomic percentage

Cr1.8 alloy	Phases	Al	Co	Cr	Fe	Ni
Dendritic regions	FeCr-rich	0.0	17.9	57.6	18.7	5.8
	NiAl-rich	33.7	18.0	7.4	10.0	30.8
Inter-dendrite regions	FeCr-rich	1.3	15.5	55.8	25.7	1.6
	NiAl-rich	35.0	16.0	7.9	11.0	30.1
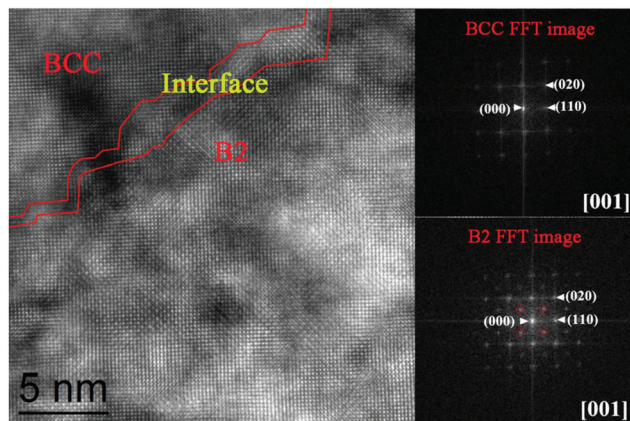
Fig. 7 HRTEM and corresponding FFT images of the BCC and B2 phases in the dendritic regions of the Cr1.8 alloy.

Fig. 9 Calculated isopleth of AlCoCr$_x$FeNi ($x = 0.4-2.4$).

a higher Cr content ($x > 1.6$). The presently investigated hyper-eutectic alloys Cr1.8, Cr2.0 and Cr2.4 are all located within the primary solidification region of A2. As predicted by the three-phase region of L + BCC_A2 + B2 in Fig. 9, all these alloys are expected to undergo the A2/B2 eutectic reaction, following the direct solidification of A2, in the late stage of solidification as the temperature drops. All this has been confirmed in the experimentally observed microstructures (Fig. 2, 3 and 8b). The inter-dendritic region (B) in the two as-cast near-eutectic alloys Cr1.8 and Cr2.0 consists of fine eutectic structures, which are similar to those observed in the eutectic alloy Cr1.6. The eutectic microstructures in Cr2.4, however, consist of large lamellas, up to 10 microns in length and are obviously different from those in the eutectic and near-eutectic alloys. The coarse microstructure in Cr2.4 is possibly due to the

higher liquidus temperature and wider gap between the precipitation temperature of the primary (A2) and the secondary (B2) phases, which facilitates a faster kinetics and longer period for the growth of eutectic structures.

In order to obtain more detailed information, such as the phase transition temperatures, phase fractions and compositions, equilibrium calculations were performed for simulating the solidification of specific alloys. Fig. 10 presents the simulation results for the alloy Cr1.8. As seen from the vertical region, the solidification starts with BCC_A2^D (corresponding to the formation of the dendritic phase, the superscript D denotes the dendritic phase), followed by the formation of the A2^E/B2^E eutectic in the inter-dendritic regions (labelled as "B" in Fig. 2, the superscript E denotes the eutectic). The solidification ends at the solidus temperature of 1356 °C. It is interesting to note that the eutectic reaction starts just 18 °C above the temperature for completion of the solidification. This indicates that the secondary phase would not have sufficient time to grow in the alloys, which should account for the ultra-fine eutectic structure in the inter-dendritic region.
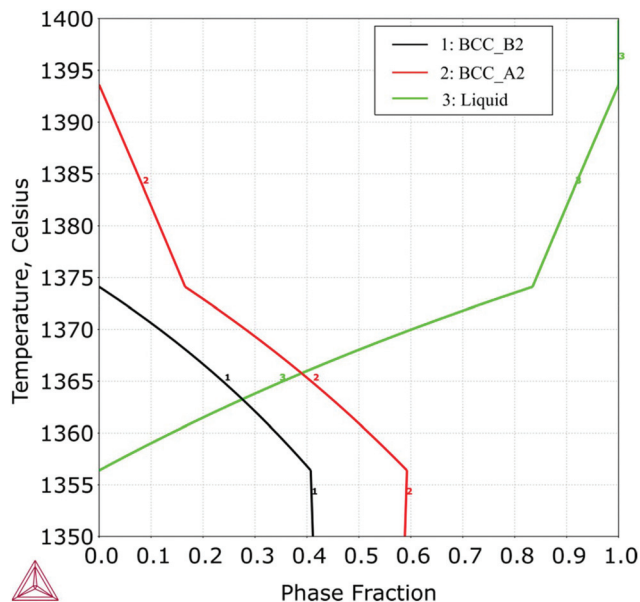

Fig. 8 SEM images of HEAs not showing a complete UFM: (a) AlCoCr$_{1.6}$FeNi and (b) AlCoCr$_{2.4}$FeNi.

Fig. 10 Equilibrium stepping calculation of the Cr1.8 alloy.

the eutectic solidification of A2^E together with B2^E, and the decomposition of the solidified B2^E (A2^{DC-E}). The microstructure in Fig. 6 seemingly indicates a spinodal mechanism in the decomposition of the as-solidified B2^E.

The averaged composition of region A from the present measurement (Table 1) could be regarded as that of the supersaturated A2 dendrites before their decomposition. With this composition known, the thermal instability of the supersaturated BCC_A2 phase can be thermodynamically studied by the equilibrium calculation. Fig. 11 shows the calculated decomposition products (*i.e.* phase assemblage expected in the dendrite region in the as-cast sample) and their corresponding compositions.

The calculation confirms not only the decomposition of the supersaturated A2 phase, but also the high fraction of B2. The amount of B2 precipitates is roughly twice that of the remaining A2 matrix phase in the dendrites, according to this calculation. Although the fraction was not quantitatively measured in the experiments, the calculated values appear to be quite reasonable, compared to the as-cast microstructure in Fig. 4a. The calculated compositions of individual phases are presented in Fig. 11b, and they can reasonably account for the experimentally measured compositions of FeCr-rich and NiAl-rich phases as given in Table 2. The agreement is remarkable despite the fact that not all the ternary subsystems in this quinary alloy system have been assessed in the thermodynamic database.

In Fig. 11b a dramatic increase of the Cr content in BCC_A2 is seen during cooling. The Cr-rich A2 phase contains 10 to 20 at% each of the Al, Co, Fe and Ni solutes at higher temperatures. The total content of these solutes decreases to about 10 at% as the temperatures drops to 600 °C where the contents of Al and Ni reach an extremely low level. The plot indicates that the decomposition of A2 accompanies the precipitation of (NiAl-rich) B2 during cooling. The plot also shows a noticeable decrease in the Cr content in the B2 precipitates. Considering the small size of the B2 precipitates, it is unlikely for secondary Cr-rich A2 precipitates to form in the primary B2 precipi-

In the present work, a large number of B2^D nano-precipitates were often observed in the as-solidified BCC_A2^D solution phase. The microstructures (in Fig. 4 and 5) indicate that the precipitation occurred *via* a nucleation mechanism. Since the particles are evenly distributed in the solution, the nucleation can be assumed to be homogeneous. The extremely high number density of the precipitates indicates that the nucleation barriers are small, which is probably due to the coherency between the B2^D precipitate and the A2^D matrix.[41] Interestingly, the as-solidified B2^E phase in the inter-dendritic region (B) also decomposed and resulted in the precipitation of BCC_A2^{DC-E} (Fig. 6, the superscript DC-E denotes the decomposed phase from the eutectic phase). It should be noted that the dark A2 phase in the region B is (see Fig. 2b & 3b) evidently formed *via* two different mechanisms, namely,
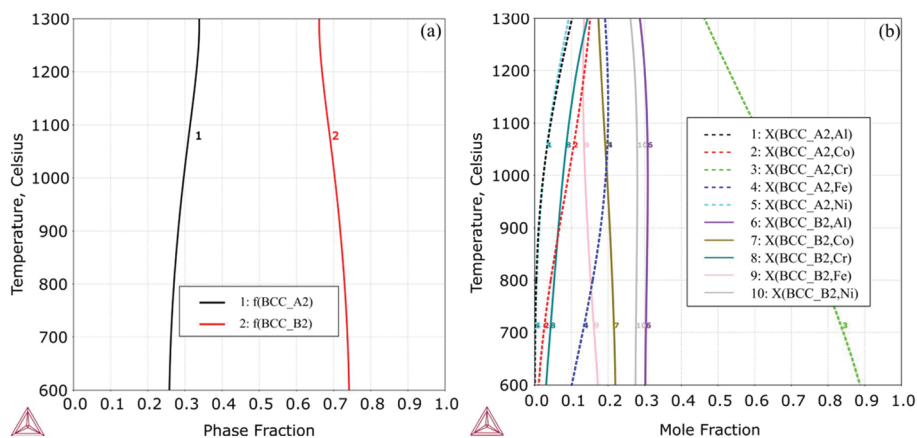

Fig. 11 Equilibrium stepping calculation of the supersaturated A2 dendrites in the Cr1.8 alloy, (a) the phase decomposition and (b) individual compositions.

tates; more likely, the primary B2 precipitates reject Cr atoms into the A2 matrix as the temperature drops. Since the calculated phase fractions and compositions noticeably vary with the temperature, the experimental results are expected to very much depend on experimental conditions and there might be micro-segregations in the phase compositions.

The supersaturated composition of the as-solidified B2 in region (B) before its decomposition is unknown. As aforementioned, the inter-dendritic region consists of fine eutectic structures; so the as-measured composition cannot be regarded as that of the supersaturated B2 phase. In order to give some clues, tentative calculations are conducted with the averaged composition. The calculation does show the decomposition of the B2 phase while the calculated phase fractions should be considered qualitative. The calculation supports our experimental observation, although it is not as decisive as that for the supersaturated A2 phase. The as-solidified B2 phase is expected to dissolve a significant amount of Cr solutes during the solidification and to reject most of them during the cooling and decomposition at sub-solidus temperatures. To save space here no additional plots (similar to Fig. 11b) are shown for B2 decomposition.

The formation of UFMs is attributed to the coupling of near eutectic alloy composition and the decomposition of supersaturated primary and secondary phases, in both dendritic and inter-dendritic regions. In order to obtain such a complete UFM in the as-cast HEAs, the following factors are important. (1) At high temperatures near liquidus one solid solution phase is stable, *i.e.* BCC (or FCC) as the primary phase. Thereafter, no intermetallic compounds precipitate. The high entropy effect could play a role here to stabilize the single solid solution phase. (2) The alloy composition is close to the eutectic composition and the temperature range between liquidus and solidus is small, to yield a fine solidification microstructure. The sluggish diffusion, although not experimentally verified for this alloy, could also contribute to the fine microstructure. (3) Both the primarily solidified and secondarily solidified solution phases decompose at low temperatures, so that coherent precipitates could form during cooling. (4) Spinodal decomposition would be an advantage for producing UFMs in the whole alloy.

Conclusions

In summary, the present work demonstrates that bulk UFM HEAs can be prepared by the direct solidification method. From the materials design point of view, the key idea of this method is, based on Calphad calculations, to locate optimal compositions which form fine eutectic microstructures followed by phase decomposition of the solidified primary and secondary phases. Practically, this design concept was exemplified by the ordinarily cast AlCoCr$_x$FeNi ($1.8 \leq x \leq 2.0$) HEAs. The introduction of phase separation (even spinodal decomposition) offers a novel strategy to prepare bulk UFM alloys in a low-cost, simple and convenient way. The present work verifies

the formation of the UFM consisting of BCC and B2 phases through continuous cooling. It sheds some light on the design of other types of UFM HEAs with desired properties, for example, UFM HEAs consisting of FCC and L1$_2$ phases, the phase constitution in nickel-based superalloys.

Experimental

Material preparation

The AlCoCr$_x$FeNi (x is the molar ratio; x = 1.8 and 2.0, denoted as Cr1.8 and Cr2.0, respectively) alloys (about 40 g each) were prepared by arc melting under a Ti-gettered high-purity argon atmosphere. The commercially pure metals (Al, Co, Cr, Fe, Ni) are above 99.9 wt% purity. The ingots were flipped and re-melted at least 5 times to improve chemical homogeneity. After that, the alloys were directly solidified in a water-cooled copper hearth.

Experimental procedure

In order to observe the microstructure, the alloy was sequentially polished and etched with ethanol diluted aqua regia at room temperature. The microstructure and composition of the alloy were investigated using a laser scanning confocal microscope (LSCM) and a scanning electron microscope (SEM, Zeiss Supra 55) equipped with an attached X-ray energy dispersive spectrometer (EDS). The phase constitution of the alloy was characterized with an X-ray diffractometer (XRD, Shimadzu XRD-6000) using a Cu-Kα target, with the scanning rate of $4° \text{ min}^{-1}$ and the 2θ scanning range of 20°–120°.

Thin foils for high-angle annular dark-field scanning transmission electron microscopy (HAADF STEM) and high resolution transmission electron microscopy (HRTEM) observations were prepared by ion milling at an ion energy of ~2 kV and an incident angle of 4°. During the ion milling process, the specimens were cooled using liquid nitrogen. The STEM observation was conducted on an FEI TECNAI F30 instrument equipped with EDS.

Conflicts of interest

There are no conflicts to declare.

Acknowledgements

References

1 H. Gleiter, *Prog. Mater. Sci.*, 1989, **33**, 223–315.

2 K. Lu, *Mater. Sci. Eng., R*, 1996, **16**, 161–221.

3 C. Suryanarayana, *Int. Mater. Rev.*, 1995, **40**, 41–64.

4 R. W. Siegel and G. E. Fougerel, *Nanostruct. Mater.*, 1995, **6**, 205–216.

5 S. C. Tjong and H. Chen, *Mater. Sci. Eng., R*, 2004, **45**, 1–88.

6 U. Erb, A. M. El-Sherik, G. Palumbo and K. T. Aust, *Nanostruct. Mater.*, 1993, **2**(4), 383–390.

7 C. C. Koch, *Nanostruct. Mater.*, 1997, **9**, 13–22.

8 R. Z. Valiev, R. K. Islamgaliev and I. V. Alexandrov, *Prog. Mater. Sci.*, 2000, **45**, 103–189.

9 R. Z. Valiev and T. G. Langdon, *Prog. Mater. Sci.*, 2006, **51**, 881–891.

10 X. Liao, Y. H. Zhao, Y. T. Zhu, R. Z. Valiev and D. V. Gunderov, *J. Appl. Phys.*, 2004, **96**, 636–640.

11 J. W. Yeh, S. K. Chen, S. J. Lin, J. Y. Gan, T. S. Chin, T. T. Shun, C. H. Tsau and S. Y. Chang, *Adv. Eng. Mater.*, 2004, **6**, 299–303.

12 B. Cantor, I. T. H. Chang, P. Knight and A. J. B. Vincent, *Mater. Sci. Eng., A*, 2004, **375–377**, 213–218.

13 Y. Zhang, T. T. Zuo, Z. Tang, M. C. Gao, K. A. Dahmen, P. K. Liaw and Z. P. Lu, *Prog. Mater. Sci.*, 2014, **61**, 1–93.

14 B. Gludovatz, A. Hohenwarter, D. Catoor, E. H. Chang, E. P. George and R. O. Ritchie, *Science*, 2014, **345**, 1153–1158.

15 L. J. Santodonato, Y. Zhang, M. Feygenson, C. M. Parish, M. C. Gao, R. J. K. Weber, J. C. Neuefeind, Z. Tang and P. K. Liaw, *Nat. Commun.*, 2015, **6**, 5964.

16 O. N. Senkov, J. D. Miller, D. B. Miracle and C. Woodward, *Nat. Commun.*, 2015, **6**, 6529.

17 Z. Li, K. G. Pradeep, Y. Deng, D. Raabe and C. C. Tasan, *Nature*, 2016, **534**, 227–230.

18 Z. Zhang, M. M. Mao, J. Wang, B. Gludovatz, Z. Zhang, S. X. Mao, E. P. George, Q. Yu and R. O. Ritchie, *Nat. Commun.*, 2015, **6**, 10143.

19 J. Y. He, H. Wang, H. L. Huang, X. D. Xu, M. W. Chen, Y. Wu, X. J. Liu, T. G. Nieh, K. An and Z. P. Lu, *Acta Mater.*, 2016, **102**, 187–196.

20 K. Y. Tsai, M. H. Tsai and J.-W. Yeh, *Acta Mater.*, 2013, **61**, 4887–4897.

21 J. Y. He, W. H. Liu, H. Wang, Y. Wu, X. J. Liu, T. G. Nieh and Z. P. Lu, *Acta Mater.*, 2014, **62**, 105–113.

22 M. C. Gao, J. W. Yeh, P. K. Liaw and Y. Zhang, *High-entropy Alloys: Fundamentals and Applications*, Springer International Publishing, Cham, Switzerland, 1st edn, 2016.

23 K. G. Pradeep, N. Wanderka, P. Choi, J. Banhart, B. S. Murty and D. Raabe, *Acta Mater.*, 2013, **61**, 4696–4706.

24 F. Otto, A. Dlouhý, C. Somsen, H. Bei, G. Eggeler and E. P. George, *Acta Mater.*, 2013, **61**, 5743–5755.

25 Y. Zou, H. Ma and R. Spolenak, *Nat. Commun.*, 2015, **6**, 7748.

26 X. D. Xu, P. Liu, S. Guo, A. Hirata, T. Fujita, T. G. Nieh, C. T. Liu and M. W. Chen, *Acta Mater.*, 2015, **84**, 145–152.

27 Z. P. Lu, H. Wang, M. W. Chen, I. Baker, J. W. Yeh, C. T. Liu and T. G. Nieh, *Intermetallics*, 2015, **66**, 67–76.

28 C. C. Kocha, *J. Mater. Res.*, 2017, **32**(18), 3435–3444.

29 Z. Fu, W. Chen, H. Wen, D. Zhang, Z. Chen, B. Zheng, Y. Zhou and E. J. Lavernia, *Acta Mater.*, 2016, **107**, 59–71.

30 F. Tian, L. Delczeg, N. Chen, L. K. Varga, J. Shen and L. Vitos, *Phys. Rev. B: Condens. Matter Mater. Phys.*, 2013, **88**, 085128.

31 Y. P. Wang, B. S. Li, M. X. Ren, C. Yang and H. Z. Fu, *Mater. Sci. Eng., A*, 2008, **491**, 154–158.

32 Y. Zhang, S. G. Ma and J. W. Qiao, *Metall. Mater. Trans. A*, 2012, **43**, 2625–2630.

33 W. R. Wang, W. L. Wang, S. C. Wang, Y. C. Tsai, C. H. Lai and J.-W. Yeh, *Intermetallics*, 2012, **26**, 44–51.

34 W. R. Wang, W. L. Wang and J.-W. Yeh, *J. Alloys Compd.*, 2014, **589**, 143–152.

35 S. G. Ma, P. K. Liaw, M. C. Gao, J. W. Qiao, Z. H. Wang and Y. Zhang, *J. Alloys Compd.*, 2014, **604**, 331–339.

36 B. A. Welk, R. E. A. Williams, G. B. Viswanathan, M. A. Gibson, P. K. Liaw and H. L. Fraser, *Ultramicroscopy*, 2013, **134**, 193–199.

37 A. Manzoni, H. Daoud, R. Volkl, U. Glatzel and N. Wanderka, *Ultramicroscopy*, 2013, **132**, 212–215.

38 J. O. Andersson, T. Helander, L. Höglund, P. F. Shi and B. Sundman, *CALPHAD*, 2002, **26**, 273–312.

39 H. L. Chen, H. Mao and Q. Chen, *Mater. Chem. Phys.*, 2017, DOI: 10.1016/j.matchemphys.2017.07.082.

40 H. Mao, H. L. Chen and Q. Chen, *J. Phase Equilib. Diffus.*, 2017, **38**(4), 353–368.

41 S. Jiang, H. Wang, Y. Wu, X. Liu, H. Chen, M. Yao, B. Gault, D. Ponge, D. Raabe, A. Hirata, M. Chen, Y. Wang and Z. Lu, *Nature*, 2017, **544**, 460–464.